DFT insights into the oxygen-assisted selective oxidation of benzyl alcohol on manganese dioxide catalysts

L. Gueci, F. Ferrante, A. Prestianni, R. Di Chio, A.F. Patti, D. Duca, F. Arena

RESEARCH HIGHLIGHTS

- The reactivity of MnO_2 catalyst in the selective aerobic oxidation of benzyl alcohol is assessed by DFT analysis
- DFT simulations predict high reactivity of defective Mn(IV) sites
- Nanostructured MnO_x catalysts show comparable activity due to the redox functionality of surface Mn(IV) sites
- 0^{th}-order kinetics disclose the remarkable influence of adsorption phenomena on the activity-stability pattern
- DFT analysis provides insights into the formation of benzoic acid, acting as *poison* of active sites

DFT insights into the oxygen-assisted selective oxidation of benzyl alcohol on manganese dioxide catalysts

L. Gueci, F. Ferrante, A. Prestianni, R. Di Chio, A.F. Patti, D. Duca, F. Arena

GRAPHICAL ABSTRACT

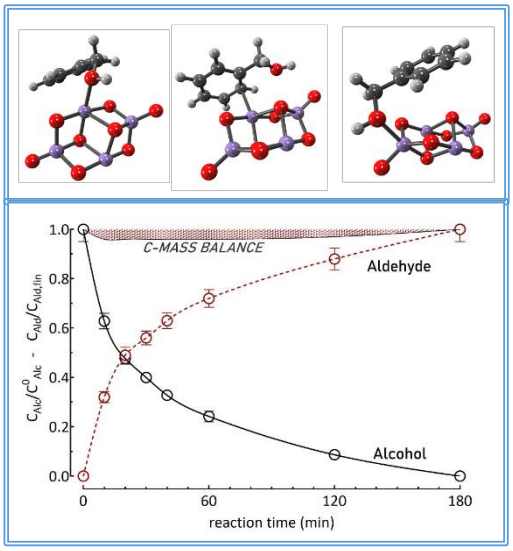

DFT analysis unveils the atomistic details of the selective aerobic oxidation of benzyl alcohol on manganese dioxide catalysts

DFT insights into the oxygen-assisted selective oxidation of benzyl alcohol on manganese dioxide catalysts

Laura Gueci [a], Francesco Ferrante [a], Antonio Prestianni [a], Roberto Di Chio [b], Antonio F. Patti [c], Dario Duca [a,*], Francesco Arena [b,*]

[a] *Dipartimento di Fisica e Chimica "E. Segrè", Università degli Studi di Palermo, Viale delle Scienze Ed. 17, 90128 Palermo, Italy*

[b] *Dipartimento di Ingegneria, Università degli Studi di Messina, Contrada Di Dio, 98166 S. Agata, Messina, Italy*

[c] *School of Chemistry, Monash University, Wellington Rd., Clayton, 3800 Victoria, Australia*

*Corresponding authors:
prof. F. Arena, e-mail: Francesco.Arena@unime.it
prof. D. Duca, e-mail: dario.duca@unipa.it

Abstract

The reactivity pattern of the MnO_2 catalyst in the selective aerobic oxidation of benzyl alcohol is assessed by density functional theory (DFT) analysis of adsorption energies and activation barriers on a *model* Mn_4O_8 cluster. DFT calculations predict high reactivity of defective Mn(IV) sites ruling a surface redox mechanism, L-H type, involving gas-phase oxygen. Bare and promoted (i.e., CeO_x and FeO_x) MnO_x materials with high surface exposure of Mn(IV) sites were synthesized to assess kinetic and mechanistic issues of the selective aerobic oxidation of benzyl alcohol on *real* catalysts (T, 333-363K). According to DFT predictions, the experimental study shows: i) comparable activity of bare and promoted catalysts due to surface Mn(IV) sites; ii) the catalytic role of oxygen-atoms in the neighboring of active Mn(IV) sites; and iii) a 0^{th}-order dependence on alcohol concentration, diagnostic of remarkable influence of adsorption phenomena on the reactivity pattern. Evidences of catalyst deactivation due to the over-oxidation of benzyl alcohol to benzoic acid, acting as *poison* of the active sites, are discussed.

Keywords:

Selective oxidation; Benzyl alcohol; MnO_2 catalyst; DFT analysis; Active sites; Reaction mechanism

1. Introduction

The conversion of alcohols to carbonyl compounds constitutes a fundamental class of industrial processes to produce numerous fine-chemicals and high-added value products. However, many of the current synthesis methods make use of expensive and noxious reagents and solvents, raising big environmental and economic concerns because of poor *atom-economy* and high *E-factor* [1]. Thus, since many years great research efforts are devoted to design of efficient solid catalysts for the selective oxidation of alcohols with oxygen, according to *Green Chemistry* guidelines [1-29]. In this context, the oxidation of benzyl alcohol is usually taken as *model* reaction because of the great relevance of benzaldehyde for dyestuff, agrochemical, pharmaceutical and perfume industries [30]. Although the superior O_2-activation functionality of noble-metals sparks the oxidation of alcoholic substrates under mild conditions [2,4-14], high costs, deactivation by *over-oxidation* and/or *fouling* of active sites, and unprecedented safety issues actually hinder their industrial exploitation. In this respect, the need of unconventional reactor designs was stressed to prevent explosion risks and corrosion phenomena [15]. By contrast, bare and promoted MnO_x materials are appealing from both the environmental and economic points of view, featuring also a significant activity-selectivity pattern in the *green* oxidation of alcohols, due to a variety of structures tuning their functionality in wide range of temperature [3,13,16-29]. However, activity loss and the need of regeneration-rejuvenation procedures are generally reported also for such catalysts [3,13,16,18-24,29]. Concerning the working mechanism, kinetic studies indicate that a typical Langmuir-Hinshelwood reaction pathway, characterized by strong adsorption phenomena, determine the activity-stability pattern of noble-metals [2,3], while the Mars-van-Krevelen mechanism provides a rough understanding of the surface reaction cycle driven by MnO_x catalysts [2,3,16,25,29]. On this account, the synergism between experiment and quantum chemistry calculation, mostly based on Density Functional Theory (DFT), can turn out essential to highlight the fundamental aspects of the catalytic reactions, assisting the design of new catalysts and the active sites optimization for a given process. In particular, cluster catalysis [31-33] is the area where this synergy manifests all its power [34,35]. In this respect, the unusual variety of structures and exotic properties of clusters are exploited to obtain new and tunable forms of catalysts, also in consideration of the high efficiency of catalysts shaped in the form of small clusters dispersed on a proper support [36-42].

Therefore, this work presents a systematic computational study of the benzyl alcohol oxidation

on a model Mn_4O_8 cluster to shed light into the mechanistic issues of the reactivity pattern of bare and promoted (i.e., CeO_x and FeO_x) manganese oxide catalysts in the *green* oxidation of benzyl alcohol to benzaldehyde. A thorough DFT analysis of the interactions of Mn(IV) centers with reagent and product molecules unveils the essential requirements of active sites and the elementary steps and intermediates accounting for the activity-selectivity-stability pattern of the studied catalysts.

2. Experimental

2.1. **Computational Analysis.** All calculations were performed in the DFT framework by using the M06-L exchange-correlation functional [43], which resulted reliable when treating inorganic compounds and when dispersion interactions may be relevant [44]. In particular, the accuracy of M06-L on determining barrier heights was already tested on a number of reactions involving transition metals [45-47], and can be quantified on the base of an averaged mean unsigned error of ca. 10 kJ mol^{-1}. The Stuttgart '97 Relativistic Small Core effective potential along with its valence double zeta basis set [48,49] was used for the Mn atoms; these was coupled with the cc-pvDZ basis set for lighter elements. The Gaussian 09 package was employed [50]. Minima and transition states related to the reaction mechanisms, in the following thoroughly discussed in terms of vibrational zero-point corrected energies, were characterized by inspection of the harmonic vibrational frequencies. Interaction energies, evaluated as the difference between the energy of the whole system and the energies of its constituents, were corrected for the basis set superposition error (BSSE) by means of counterpoise procedure [51].

2.2. **Catalyst preparation.** The bare (M) and Ce (M3C1) or Fe (M3F1) promoted MnO_x catalysts were prepared by the *redox-precipitation* technique consisting of the titration in acidic solution (pH, 4.5±0.5) of the $Mn(NO_3)_2{\cdot}4H_2O$ and/or $FeSO_4{\cdot}7H_2O$ precursors with aqueous solutions (0.2 L) of $KMnO_4$-$Ce(NH_3)_2(NO_3)_6$. After titration, the solids were digested, filtered, washed with hot distilled water, dried at 373 K (16 h) and further calcined in air at 673 K (6h) [22,52].

2.3. **Catalyst characterization.** X-ray fluorescence (XRF) analyses were performed to determine the chemical composition of the catalysts. Surface area (SA), pore volume (PV) and average pore diameter (APD) data were obtained by elaboration of nitrogen adsorption isotherms (77K) by the BET and BJH methods, respectively. X-ray diffraction (XRD) data in the range of 10-80° were obtained at scan rate of $6°{\cdot}h^{-1}$ using the Ni β-filtered Cu K_α radiation (40 kV; 30 mA). X-ray Photoelectron Spectroscopy (XPS) data were obtained by a spectrometer operating with a monochromatized Al-K_α radiation (300 W). The B.E.

regions of C_{1s}-K_{1s} (280-300 eV), O_{1s} (525-535 eV), Mn_{2p} (635-680 eV), Fe_{2p} (700-740 eV) and Ce_{3d} (870-935 eV) were calibrated taking the C_{1s} line of adventitious carbon (284.8 eV) as reference. Temperature Programmed Reduction analyses in the range of 293-773K were performed using a quartz reactor (w_{cat}, 20 mg), heated at the rate of 12K·min^{-1} and fed with a 5% CO/He (CO-TPR) carrier (F, 60 *stp* mL·min^{-1}) [22]. The patterns are normalised to the MnO_x content of the samples (Table 1).

2.4. **Catalyst testing.** Catalytic tests in the aerobic liquid phase oxidation of benzyl alcohol (BA) with oxygen were carried out into a 3-necked pyrex glass flask reactor containing a toluene solution (V_{tot}, 50 mL) of benzyl alcohol and ethyl benzoate as internal standard. Benzyl alcohol concentration was varied between 0.04 and 9.70 mol·L^{-1}, the latter corresponding to the absence of solvent. The suspension was stirred and heated at the reaction temperature in O_2 flow (60 *stp* mL·min^{-1}) adding, then, powdered catalyst samples corresponding to concentrations going from 0.4 to 49 g·L^{-1} [22,29].

3. Results and Discussion

3.1. Modeling approaches

3.1.1. Why the Mn_4O_8 cluster? The catalytic model on which the oxidation reaction of benzyl alcohol was simulated is a Mn_4O_8 cluster, tailored from a pyrolusite lattice. Its geometry was optimized in all possible spin multiplicity states having values ranging in-between 1 and 17 (i.e., ranging the S value in-between 0-8). The results obtained revealed that Mn_4O_8 in its most stable state has 12 unpaired electrons. Intermediate species and transition states belonging to the reactions mechanism were explored taking into account possible spin coupling/uncoupling by considering one unit either lowering or increasing, starting from the multiplicity value of the pristine Mn_4O_8 cluster (i.e., 13). In its most stable spin multiplicity state, Mn_4O_8 has a C_{2h} symmetry, hence two different coordinatively unsaturated (CUS) Mn sites, and three not equivalent O-atoms characterize the model, as shown in Figure 1. In passing, it is to be underlined that the dangling oxygen (O1) atoms showed a peculiar behaviour, being not involved in the starting reaction path. However, it was observed that other dangling oxygen atoms (O1c) could be formed along the reaction path (*v. infra*), resulting basic for closing the catalytic loop through the production of a water molecule. Notably, the model Mn_4O_8 cluster is representative of the CUS Mn(IV) sites present at the surface of MnO_x catalysts considered in the study (*v. infra*).

In fact, given the number of atoms considered in the Mn_4O_8 cluster and the stoichiometry of pyrolusite — beyond the actual computational optimizations performed, which confirm the

following inference — it is not possible to find a higher symmetry or a different topology for the suggested model. In addition, the experimental evidences relating to the structural and kinetic characterizations previously carried out on the catalysts simulated in this study [22,29,52] clearly show, either for bare or promoted MnO_x catalysts, a very high dispersion of the MnO_2 phase and a catalytic activity attributable to quasi-monodisperse catalytic nanoformations, straightforwardly compatible with the Mn_4O_8 model. That the suggested model is heuristic, in any case, is confirmed by the adsorption results of the reagents and products, of the oxidation process, studied on a double-sized cluster, Mn_8O_{16}, treated at the same level of calculation as the smallest one. These indeed showed i) variations in the multiplicity of spin consistent with the increase of the cluster size, ii) similar trends in the adsorption energetics and, in some cases, iii) deviations in the absolute adsorption values lower than 2%, as shown in Fig. S1 of SI.

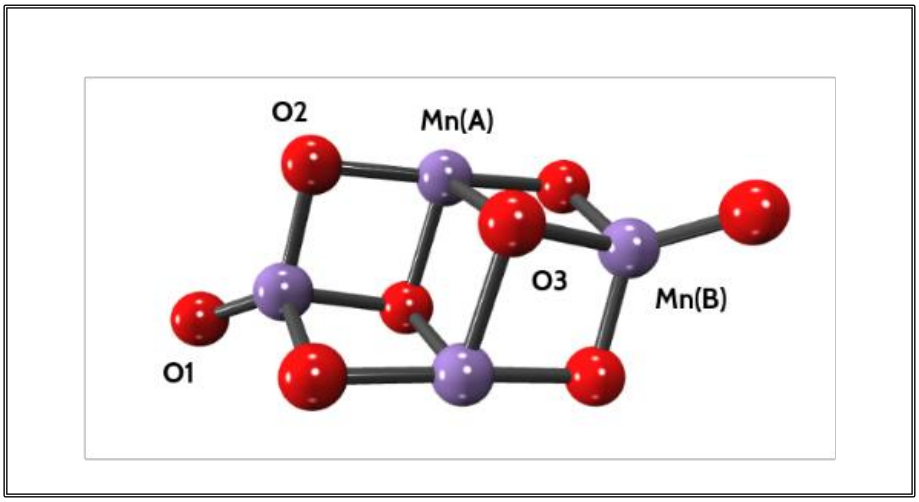

Figure 1. The Mn_4O_8 cluster geometry, optimized in the $2S + 1 = 13$ spin multiplicity state. Non-equivalent centers' labeling used throughout the text is shown.

3.1.2. Benzyl alcohol adsorption. At first, different adsorption geometries of benzyl alcohol on Mn_4O_8 were tested. The benzyl alcohol molecule can either interact with the two Mn sites of the catalyst by its oxygen atom, leading to the O-Mn(A) and O-Mn(B) adducts respectively, or by the phenyl group, forming the C_6H_5-Mn(A) adduct. In passing, it has here to be stated that the same nomenclature will be in the following employed to label the reaction mechanisms arising from the three homonym adsorption geometries. Both O-Mn(A) and C_6H_5-Mn(A) adducts exhibit side interactions, while in the O-Mn(B) adsorption geometry the phenyl group partially lies above the

cluster. In all cases, however, the most stable spin-state configuration was found to be 13, as already found for the isolated cluster. The three adsorption geometries are shown in Figure 2. The relevant Mn-O distances involving the alcohol group are 2.13 and 2.10 Å in O-Mn(A) and O-Mn(B), respectively, while 2.35 Å is the distance between Mn(A) and the closest carbon atom belonging to the phenyl group in C_6H_5-Mn(A). According to these findings, the most stable system is O-Mn(A), with a BSSE corrected interaction energy of -128.0 kJ mol^{-1}, followed by the other A site adsorption (-96.6 kJ mol^{-1}). Much less favorable (-58.5 kJ mol^{-1}) is the alcoholic oxygen interaction with the Mn(B) site. To evaluate feasible structural changes in the alcohol molecule after the adsorption, O-CH_2 and O-H bond distances were analyzed. As expected, an O-CH_2 bond distance elongation (~1.45 Å) in the O-Mn(A) and O-Mn(B) adsorbates with respect to the isolated benzyl alcohol (1.41 Å) was observed, highlighting the oxygen interaction with the catalyst. Whereas, in the C_6H_5-Mn(A) case no changes were recorded. Also, the O-C-C-C dihedral angle value (ϑ) allows one to distinguish among the adsorption geometries: ϑ is, indeed, equal to 142° and 70° in O-Mn(A) and O-Mn(B), where the O atom interacts with Mn, while is almost 0° (as for isolated alcohol) in C_6H_5-Mn(A). The alcohol geometry distortion in O-Mn(B) is likely responsible for the weak adsorption energy, since a strong repulsion between H-atoms of phenyl and CH_2 group is evident. Finally, it is noteworthy that the adsorption did not affect the O-H bond length, being its value unchanged in all the cases.

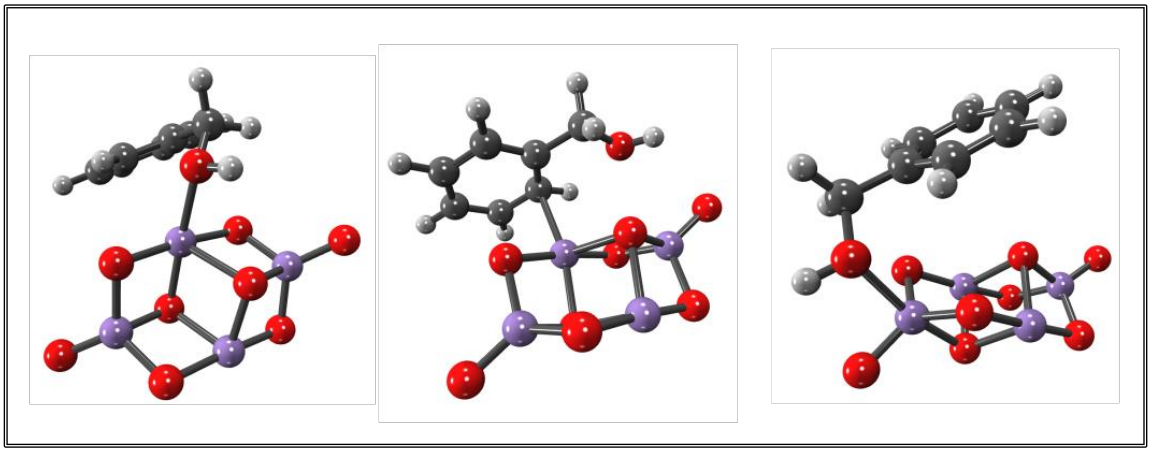

Figure 2. From left to right, the O–Mn(A), C_6H_5–Mn(A) and O–Mn(B) adsorption modes of the benzyl alcohol molecule on the Mn_4O_8 cluster.

3.1.3. Benzaldehyde formation. Once benzyl alcohol is adsorbed, its oxidative dehydrogenation takes place, forming a benzaldehyde molecule and leaving two H-atoms on the Mn_4O_8 cluster.

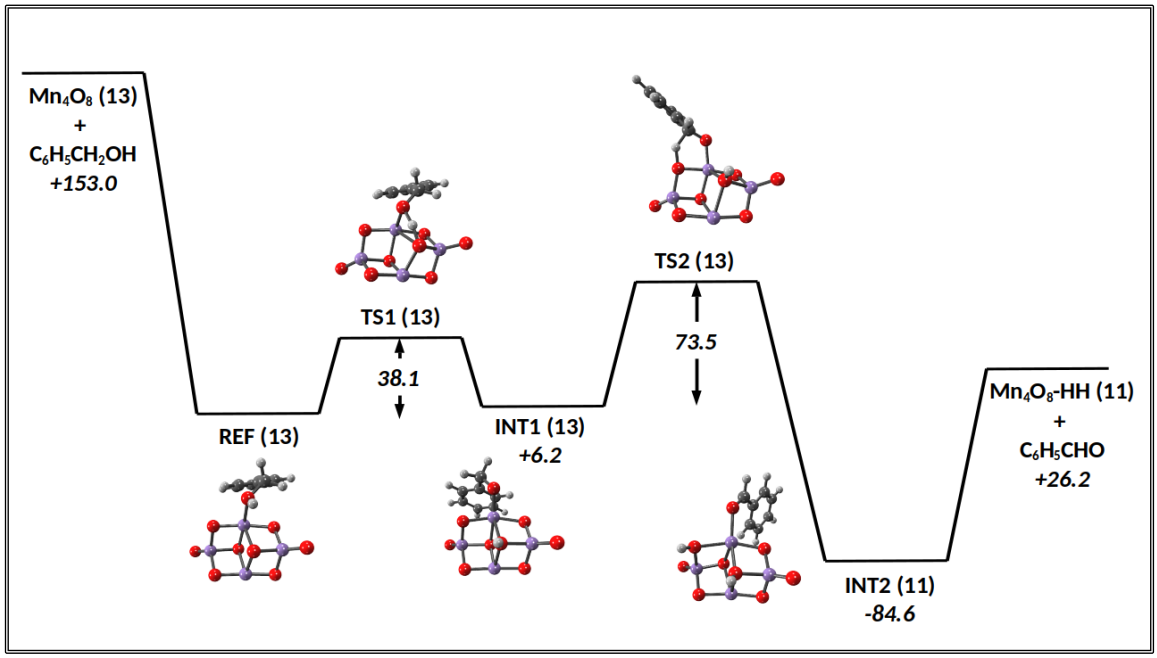

Figure 3. Oxidation of benzyl alcohol to benzaldehyde on the Mn_4O_8 cluster, occurring through the O-Mn(A) mechanism. Energies of the starting reactants, minima and final products are relative to that of REF species, while the energy barriers are calculated with respect to the energies of the species preceding the corresponding transition states. Spin multiplicity for each species is reported in parentheses. All values are expressed in kJ mol^{-1}.

The first step in the O-Mn(A) reaction pathway (reported in Fig. 3) is the hydroxyl hydrogen transfer to the O3 atom of the catalyst, a process having an energy barrier of 38.1 kJ mol^{-1}. The resulting intermediate is found to be slightly less stable than the reactant. For the second hydrogen loss, a peculiar molecular orientation is required. In fact, once a CH_2 hydrogen is directed towards the O2 atom, the generation of an adsorbed benzaldehyde molecule can be observed, in turn resulting by the previous formation of the transition state TS2, characterized by an energy barrier of 73.5 kJ mol^{-1}. It is interesting to notice that the multiplicity spin state of the system, from the value of 13 decreased to 11. Providing 110.8 kJ mol^{-1} of energy, benzaldehyde desorbs and the remaining Mn_4O_8-HH hydrogenated species must be dehydrogenated in order to restore the pristine catalyst, hence closing the catalytic cycle. This topic is discussed in the next paragraph.

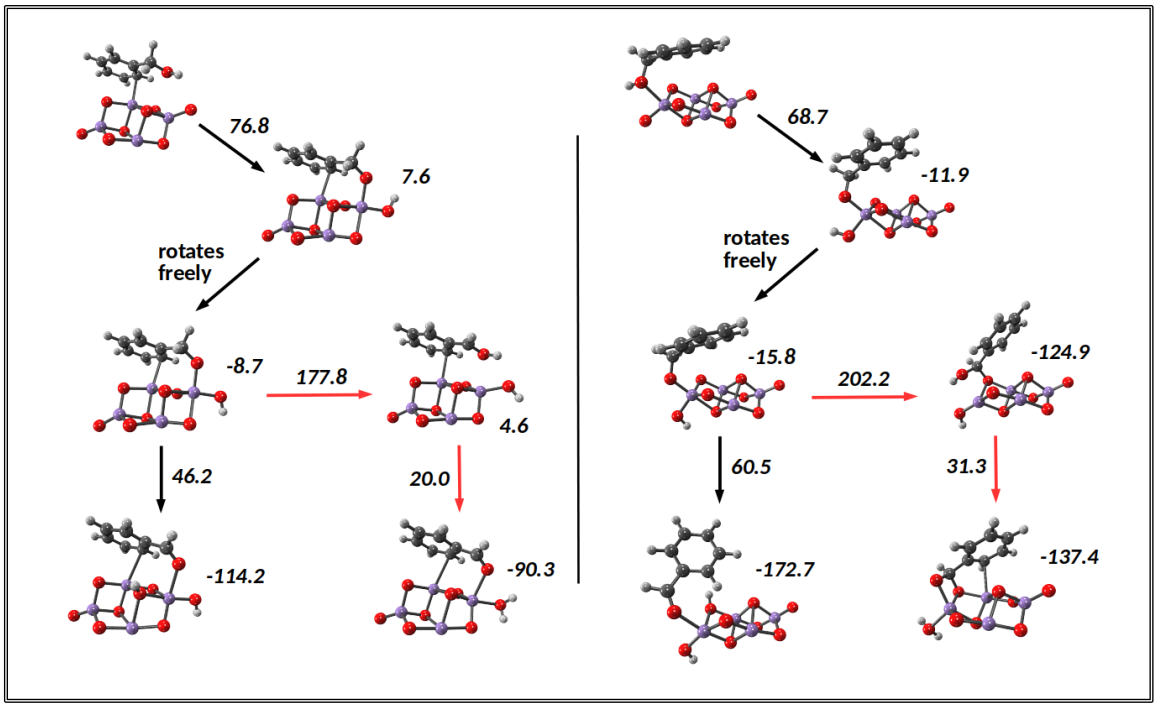

Figure 4. Oxidation of benzyl alcohol to benzaldehyde on the Mn_4O_8 cluster, occurring through the C_6H_5–Mn(A) and O–Mn(B) mechanisms (left and right panel, respectively). Energies of the optimized minima are relative to that of the starting reactants. The energy barriers are reported near the arrows. The paths connected by the red arrows are kinetically forbidden. All values are expressed in kJ mol^{-1}.

The C_6H_5-Mn(A) and O-Mn(B) pathways are collected in Figure 4. The C_6H_5-Mn(A) oxidation route implies, at first, the hydroxyl-hydrogen transfer to the O1 atom, overcoming an energy barrier of 76.8 kJ mol^{-1}. After the O1-H group freely rotates, the reaction can proceed in two different ways. The first possibility is the direct transfer of the CH_2 hydrogen to the catalyst O3 site, with an energy barrier of 46.2 kJ mol^{-1}. The benzaldehyde-Mn_4O_8-HH adduct is found to be in spin multiplicity state of 15. Alternatively, one hydrogen atom could be subjected to intramolecular migration from CH_2 to the alcoholic oxygen and subsequently transferred to O1. Thus, co-adsorbed benzaldehyde and water would be formed. Yet, if compared to the direct hydrogen loss, the energy barrier associated with the intramolecular process is too high (177.8 kJ mol^{-1}) and, as a consequence, this pathway was not further considered.

Also the last investigated O-Mn(B) reaction mechanism begins with the hydroxyl hydrogen transfer to the O1 atom, overcoming an energy barrier of 68.7 kJ mol^{-1}. As for the C_6H_5-Mn(A) case, both the direct CH_2 hydrogen transfer to the catalyst and the intramolecular H-shift, followed by the H_2O formation were observed. Once again the first was found to be strongly preferred, being the energy

barriers for the two processes 60.5 and 202.2 kJ mol^{-1}, respectively. The O-Mn(A) path, characterized by the highest interaction energy and involving the lowest energy barriers, was finally considered to be the most likely to occur during the benzyl alcohol oxidation to benzaldehyde on the Mn_4O_8 cluster. Hence, it was the only mechanism further investigated.

3.1.4. Formation of the intermediate Mn_4O_9 cluster. To restore the oxidized form of the catalyst originated from the O-Mn(A) mechanism, the desorption of an H_2 molecule was initially hypothesized. However, the H-H distance (≈3.8 Å) is too large for the two atoms to directly interact and bond. As a consequence, hydrogen hopping steps to Mn or O atoms were taken into consideration. However, according to the found energy barriers that are higher than 120 kJ mol^{-1}, also the hopping process could be regarded as kinetically unfavorable. Since the modeling approach mimics the experimental process carried out under oxygen flow, the adsorption of one O_2 molecule on the Mn_4O_8-HH intermediate was hypothesized. A μ^1 geometry on the Mn(A) was observed and the interaction energy was calculated to be -67.7 kJ mol^{-1}. Figure 5 details the proposed mechanism for the transformation of Mn_4O_8-HH in aerobic conditions. First, the O2-bounded hydrogen moves to the nearest dangling oxygen atom, with an energy barrier of 33.1 kJ mol^{-1}. Next the second hydrogen is transferred to the same oxygen atom, crossing an energy barrier of 60.8 kJ mol^{-1}, with the subsequent formation of one water molecule. The desorption of the latter was found to require 118.7 kJ mol^{-1}. The catalytic cycle however is not closed yet, since the residual fragment, Mn_4O_9, has an extra oxygen atom with respect to the starting Mn_4O_8 cluster. The reaction of the Mn_4O_9 with a second alcohol molecule will be discussed in the next paragraph.

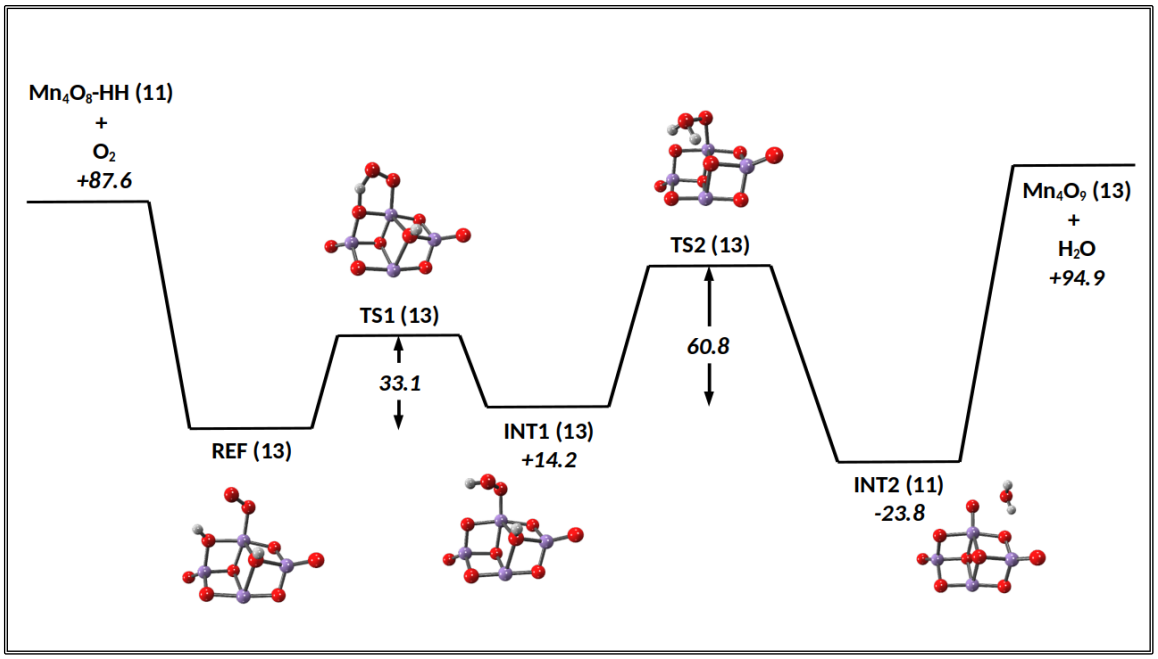

Figure 5. Reaction path characterizing the aerobic formation of one H_2O molecule and the intermediate Mn_4O_9 cluster. Energies of the starting reactants, minima and final products are relative to the REF species. Energy barriers are calculated with respect to the energy of the species preceding the corresponding transition states. Spin multiplicity of each optimized system is reported in parentheses. All energy values are expressed in kJ mol^{-1}.

3.1.5. Third step: benzyl alcohol oxidation on Mn_4O_9. In order to mimic this step, three different adsorption sites of benzyl alcohol on the Mn_4O_9 cluster were considered, as the two Mn(A) atoms are now not equivalent. For the sake of clarity, the Mn site of the Mn_4O_9 cluster bonding the extra O-atom is relabeled Mn(C) while O1c now denotes the just mentioned extra oxygen atom. As a matter of fact, the O-Mn(C) adsorption geometry was found to be the most stable, with a BSSE corrected interaction energy of -167.5 kJ mol^{-1} and a spin multiplicity which decreased to 11 after adsorption. The O-Mn(B) and O-Mn(A) follow in the order, being the interaction energies -154.2 and -137.5 kJ mol^{-1}, respectively. The proposed reaction mechanism on Mn_4O_9 is shown in Figure 6. The hydroxyl hydrogen is transferred to the O1c atom, requiring the overcoming of an energy barrier of 53.3 kJ mol^{-1}; afterwards, a negligible energy barrier of 7.3 kJ mol^{-1}, associated with the CH_2 hydrogen transfer to the same O1c, transforms INT1 to INT2, that is benzaldehyde and water co-adsorbed on the restored Mn(A) site of the Mn_4O_8 cluster. Desorption energy for both benzaldehyde and water was calculated to be 231.7 kJ mol^{-1}, whereas benzaldehyde removal from the hydrated cluster requires only 93.3 kJ mol^{-1}. This last process closes the catalytic cycle on the

Mn_4O_8 cluster, which transforms two benzyl alcohol molecules into two benzaldehyde and two water molecules, with a calculated Gibbs free energy difference of -181.4 kJ mol^{-1}. However, these data also lead to infer that an over-oxidation of benzyl alcohol to benzoic acid could take place before benzaldehyde desorbs [29]. These topics deserve further investigations to unveil the role of water during the formation of benzaldehyde and of oxygen from both gas-phase and catalyst in the over-oxidation processes [29].

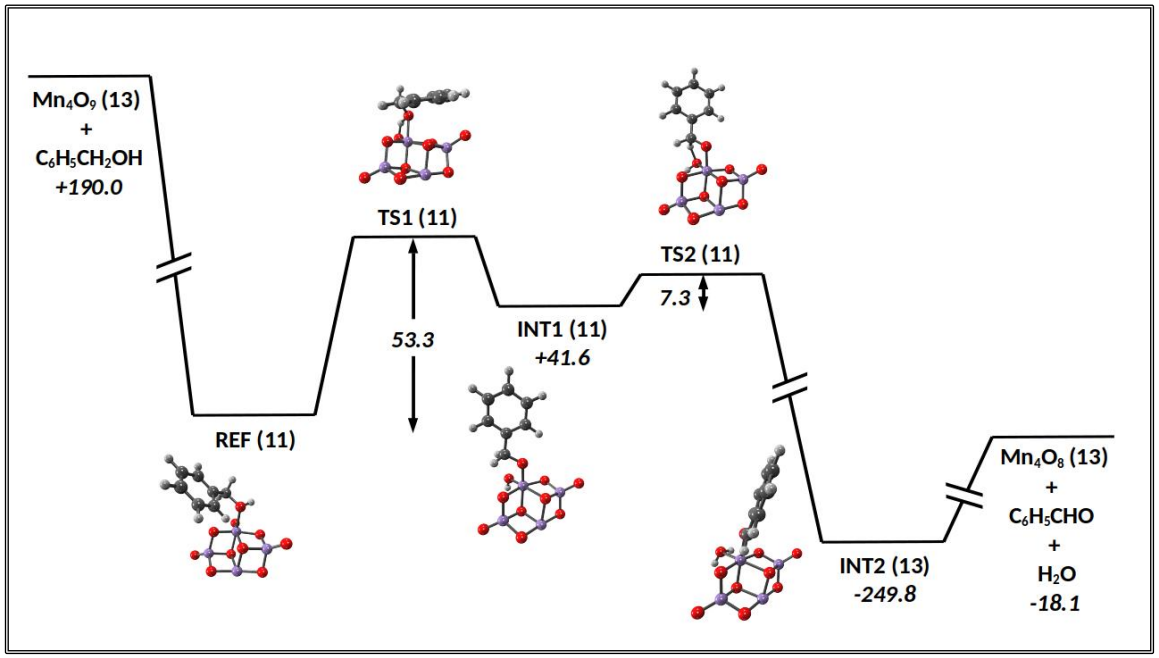

Figure 6. The O-Mn(C) mechanism, outlining the second benzyl alcohol molecule oxidation to benzaldehyde on the over-oxidized Mn_4O_9 cluster, which restores the Mn_4O_8 starting catalyst and forms with benzaldehyde also a water molecule. Energies of the initial reactants, minima and final products are relative to the energy of the REF species while the energy barriers are referred to those of the species preceding the corresponding transition states. Spin multiplicity for each species is reported in parentheses. All energy values are expressed in kJ mol^{-1}.

3.2. Experimental findings

3.2.1. Catalyst structure and redox properties. Bare and promoted (i.e., CeO_x and FeO_x) MnO_x materials were prepared by redox-precipitation reactions of suitable precursors, because of the recognized efficiency of the technique to promote the oxide dispersion and the formation of oxide nanodomains exposing Mn(IV) sites with size and structure comparable to the model Mn_4O_8 cluster [22,52,53]. The main physico-chemical properties of the catalysts (Table 1) and forthcoming

characterization data support this assumption, strengthening the consistency of the study.

First, the XRD data in Figure 7 show that the addition of promoters hinders any crystalline MnO_x structure in the promoted systems. At variance, the bulk M system displays a set of peaks consistent with the XRD pattern of α-MnO_2 and/or cryptomelane-type structures (JCPDS 44-0141) [22,25,28,52,54,55]. Indeed, chemical composition data indicate a K/Mn atomic ratio of 0.13 (Table 1), which is typical of tunnel-structured α-MnO_2 species (i.e., KMn_8O_{16}) [25,54,55]. Ceria promoted catalyst misses such peaks, showing some broad reflexes of ceria nanoparticles and a small peak at ~37° due to the incipient genesis of MnO_2 nanodomains [22,52]. Absence of cerianite reflexes and amorphous structure of the iron-oxide phase render in fact more evident two peaks at ~37° and ~66° in the XRD pattern of the M3F1 material, also ascribable to the nascent MnO_2 phase.

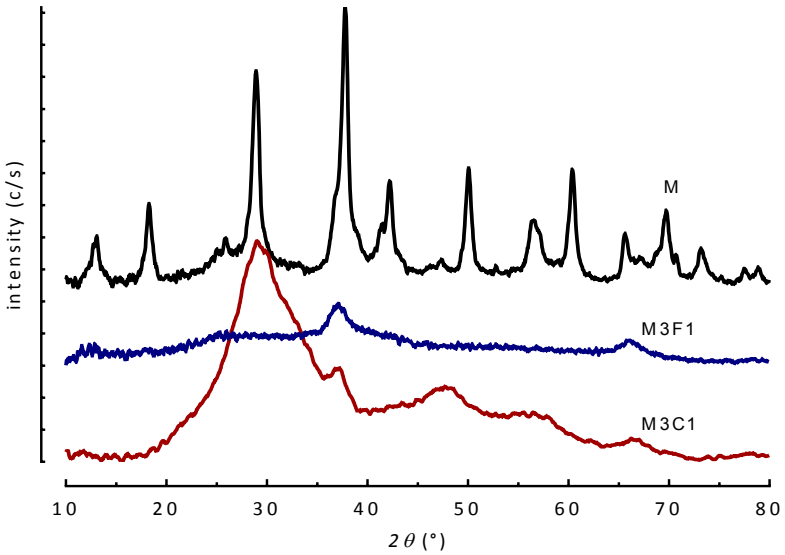

Figure 7. XRD patterns of the studied catalysts.

The substantial lack of long-range crystalline order of M3C1 and M3F1 materials proves the effective role of ceria and iron oxide as structural promoters favoring the dispersion of the MnO_x phase and surface area values considerably larger than the bulk M system (Table 1). Despite the M3C1 catalyst has the largest surface area (184 $m^2 \cdot g^{-1}$) and pore volume (0.57 $cm^3 \cdot g^{-1}$), all the systems are characterized by similar mesoporous texture and average pore diameter (27-31 nm).

Moreover, XPS characterization data signal a negligible influence of promoters on the chemical properties of the MnO_x phase (Fig. 8). Indeed, XPS data indicate surface concentrations of Mn, Ce and Fe matching the composition of promoted catalysts (Table 1), supporting XRD evidences on the

high dispersion of the oxide phases. Further, unchanging center position of the $Mn_{2p1/2}$ peak (642.2 ±0.2 eV) and spin-orbit splitting value of $Mn_{2p1/2}$-$Mn_{2p3/2}$ peaks (11.8 eV) unveil the prevalent contribution of surface Mn(IV) atoms (60-85%), irrespective of composition. Indeed, the promoted catalysts feature similar average oxidation number (AON) of surface Mn atoms (+3.76/+3.82), slightly lower than the bulk M sample (+3.92), while the crucial influence of surface Mn(IV) sites on the oxidation activity is evident from the CO-TPR patterns in Figure 8. These show two peaks at 453K and 603K for Ce- and Fe- promoted systems, which shift upward for the bulk MnO_2 sample (518K and 653K). Namely, the first peak monitors the reduction of surface-subsurface Mn(IV) atoms, while the smaller peak at higher temperature accounts for the final reduction of minor amounts of Mn_2O_3-Mn_3O_4 species to MnO [22,52,53]. In the light of above data, the upward shift of the first peak reflects a higher crystallinity of MnO_2 domains of the bulk material and, thus, lower exposure and defectivity of surface Mn(IV) centers in comparison to promoted systems. While, minor changes in the onset reduction (303-323K) rule out significant *chemical effects* of promoters on the reactivity of surface Mn(IV) sites [22,52,53]. Moreover, considering that the CO consumption at T>673K of the M3F1 catalyst is due to the incipient reduction of Fe(III) ions, the peak area indicates extents of CO consumptions (CO_{mol}/Mn_{at}, 0.87-1.0) consistent with the AON probed by XPS analysis (Table 1). Thus, CO-TPR data reveal an easy catalyst reducibility due to the reactivity of O-atoms in the neighboring of surface Mn(IV) atoms, likely constituting the defective sites (e.g., CUS) of MnO_2 nanodomains. Thus, high reactivity toward CO, structure and surface properties of the catalysts suggest that surface Mn(IV) sites, similar to the model Mn_4O_8 cluster of computational analysis, shape the redox functionality of bare and promoted catalysts.

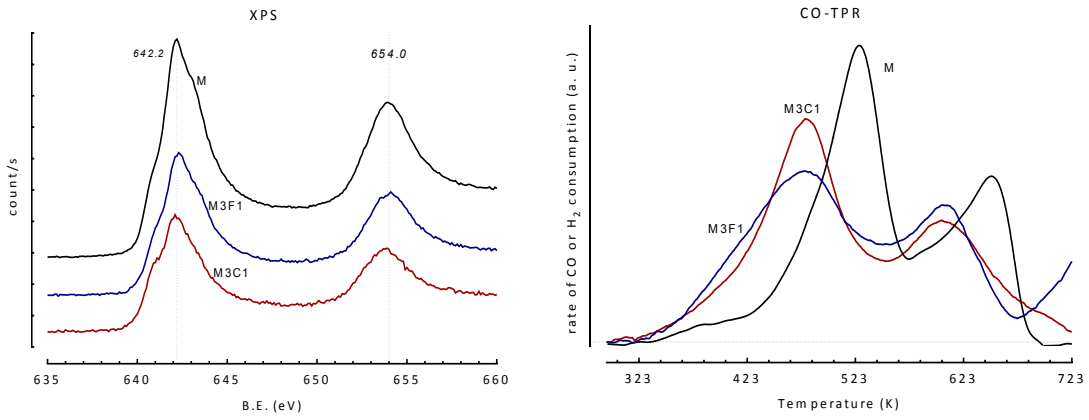

Figure 8. XPS Mn spectra (left) and CO-TPR profiles (right) of the studied catalysts.

3.2.2. Activity pattern. The concentration profiles of benzyl alcohol and benzaldehyde, recorded with bare and promoted catalysts during 3h of reaction time (T, 343K), depict specular exponential trends, accounting for a complete conversion of benzyl alcohol to benzaldehyde, similarly to what observed for the bare MnO_2 catalyst (Fig. 9).

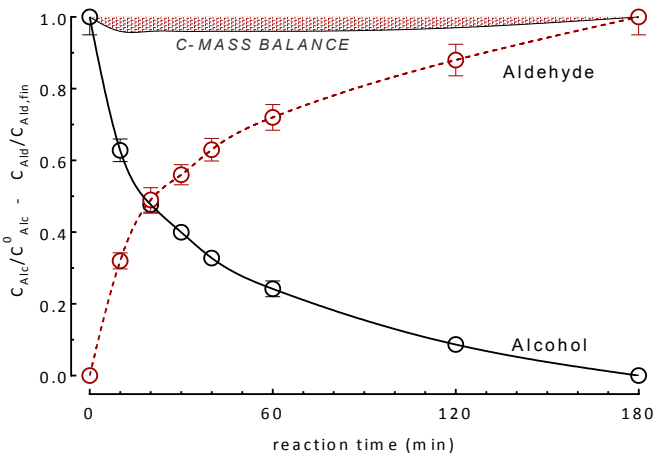

Figure 9. Benzyl alcohol and benzaldehyde concentration and C-mass balance *vs.* reaction time with the bulk M catalysts (T, 343K; V, 50 mL; V_{Alc}, 0.5 mL (4.86 mmol); w_{cat}, 0.45 g; F_{O2}, 60 mL·min^{-1}; P, 1 atm).

A reliable C-mass balance proves that adsorption phenomena do not affect the alcohol conversion and that benzaldehyde is the sole reaction product. Indeed, under the same conditions, the M3C1 catalyst drives the oxidation of benzaldehyde with much slower rate, reaching a conversion of 5% in 5h. These evidences rule out the occurrence of nucleophilic oxidation paths, substantiating the electrophilic character of active oxygen species (i.e., O_2^-, $O_2^=$) involved in the surface reaction (*v. supra*). Analogous activity-selectivity patterns and kinetic data in Figure 10 confirm that the promoters do not affect the functionality of surface active Mn(IV) sites (*v. supra*) [22,52,53]. In fact, mirroring the effects of MnO_x loading and dispersion, all the catalysts show similar rate values in the range of 333-363K (Fig. 10A). However, referred to surface area, the bulk M sample features the highest activity (Fig. 10B), due to the largest exposure of Mn(IV) sites, while the promoted catalysts feature analogous MnO_x-site activity values (e.g., TOF), systematically higher than the bulk M system (Fig. 10C), owing to higher MnO_x dispersion and no chemical effects of promoters (*v. supra*). Anyway, unchanging activation energy values (E_{app}, 52-57 kJ·mol^{-1}) strengthen the evidence that the functionality of the catalysts in the selective oxidation of benzyl alcohol depends on the reactivity of surface Mn(IV) centers, irrespective of composition.

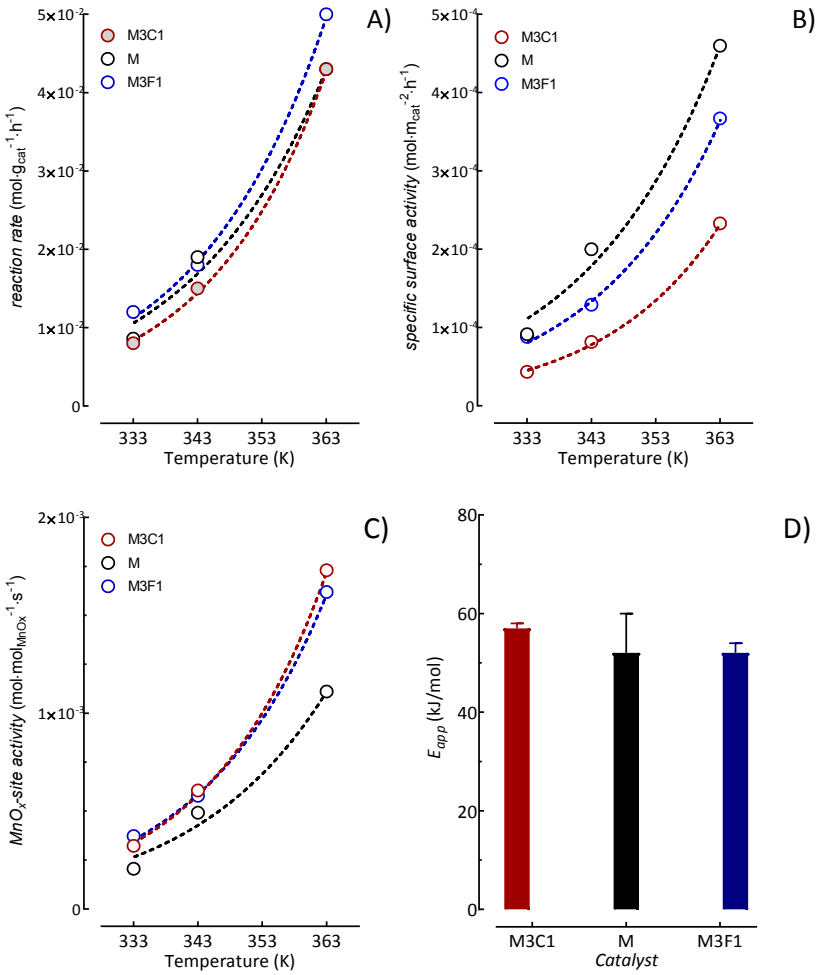

Figure 10. Rate (X_{Alc}<*20%*), specific activity and apparent activation energy values of M, M3C1 and M3F1 catalysts in the selective oxidation of benzyl alcohol in the range of 333−363K.

3.2.3. Mechanistic evidences. The reliability of DFT predictions on the reaction path driven by the model Mn_4O_8 cluster was definitively ascertained by the following kinetic-mechanistic findings. Despite the concentration trends of reagent and product during time apparently suggest 1st-order kinetics on alcohol concentration (Fig. 9), a set of measurements ($X_{Alc}\rightarrow 0$) varying alcohol (0.04-9.7 mol·L^{-1}) and catalyst (0.4-49 g·L^{-1}) concentration (Tab. S1 of SI) shows, in fact, unchanging rate values (0.019±0.002 mol$_{Alc}$·g$_{cat}^{-1}$·h^{-1}) denoting rather a 0th-order dependence (Fig. S2 of SI) [29]. Since an over-reduction of the catalysts can be ruled out (*v. infra*), these peculiar kinetics are diagnostic of a Langmuir-Hinshelwood type reaction path, rate limited by adsorption-desorption processes of reactants and products (*r.d.s.*) [29], as suggested by the energy barriers calculated by DFT analysis.

In fact, the role of catalyst oxygen and gas-phase O_2 on the surface reaction path was assessed comparing the activity data of the studied catalysts in absence and in the presence of oxygen [29]. Considering that similar results were obtained in all the cases, in particular, the M3C1 catalyst drives the oxidation of benzyl alcohol in absence of gas phase O_2 (i.e., N_2 flow), attaining a conversion degree in the first five minutes (10-15%) similar to that in O_2 (Fig. S3 of SI). The conversion rises slowly to 25% in the successive 10 min, keeping thereafter unchanged during 4h, while the presence of oxygen favors a full alcohol conversion after ca. 3h. Therefore, these findings prove that catalyst surface oxygen species spark the oxidation of the substrate, mimicking the first step of the oxidation of the first benzyl alcohol molecule on the Mn_4O_8 cluster (Fig. 3). However, considering that the produced aldehyde (0.6 mmol) corresponds to an oxygen consumption much lower than catalyst lattice oxygen (~3 mmol) and that O_2 flow restores an activity level comparing to that recorded in a 2^{nd} reaction cycle (Fig. S3 of SI), it can be argued that the studied catalysts drive a *surface redox* path, sustained by gas phase oxygen. According to DFT prediction, this accomplishes the oxidation of the 2^{nd} alcohol molecule with formation of water molecule and the replenishment of the active site (Figs. 5 and 6).

At this stage, the only apparent inconsistence of experimental data relies in the shape of conversion trends (Fig. 9), clearly mismatching the 0^{th}-order kinetics on benzyl alcohol concentration (Fig. S2 of SI). This can be explained by our previous findings, indicating an ongoing catalyst deactivation due to the slow formation of benzoic acid, poisoning the active sites [29]. In this respect, the negligible benzaldehyde oxidation functionality of the catalysts coupled to DFT data on the energy of water-benzaldehyde desorption (*v. supra*) suggest that the formation of benzoic acid is not due to a typical Mars-van Krevelen path. However, the molecular aspects of acid formation and catalyst deactivation are out of the scopes of the present work, being the topics of ongoing theoretical evaluations and experimental studies.

4. Conclusions

A DFT analysis of a *model* Mn_4O_8 catalyst in the selective oxidation of benzyl alcohol with O_2 has been performed.

Bare and promoted MnO_x catalysts with high dispersion of surface Mn(IV) sites were prepared and tested in the selective oxidation of benzyl alcohol for comparative purposes.

DFT analysis of the interactions of reagent and product molecules with Mn(IV) sites indicates five elementary steps accounting for the activity-selectivity-stability pattern of the MnO_2 catalysts.

The most intimate atomistic issues of the catalytic process indicate a typical L-H type mechanism leading to benzaldehyde formation:

$$\sigma O + C_6H_5\text{-}CH_2OH \leftrightarrows \sigma O\cdots OHCH_2\text{-}C_6H_5 \quad (1),$$

$$\sigma O \cdots OHCH_2\text{-}C_6H_5 \leftrightarrows \sigma O(H)_2 + C_6H_5\text{-}CHO \quad (2),$$

$$\sigma O(H)_2 + O_2 \leftrightarrows \sigma O\text{-}(H)_2\cdots O_2 \quad (3),$$

$$\sigma O\text{-}(H)_2\cdots O_2 \leftrightarrows \sigma O\text{-}O + H_2O \quad (4),$$

$$\sigma O\text{-}O + C_6H_5\text{-}CH_2OH \leftrightarrows \sigma O\text{-}O\cdots C_6H_5\text{-}CH_2OH \quad (5),$$

$$\sigma O\text{-}O\cdots C_6H_5\text{-}CH_2OH \leftrightarrows \sigma O + H_2O + C_6H_5\text{-}CHO \quad (6),$$

where σO and $\sigma O\text{-}O$ represent the pristine and per-oxidized forms of the Mn(IV) site of the model Mn_4O_8 cluster.

Catalyst deactivation phenomena are due to the consecutive oxidation of benzaldehyde to benzoic acid, acting as *poison* of the active Mn(IV) sites.

The role of adsorbed water and the oxygen species leading to the formation of benzoic acid are the topics of ongoing theoretical and experimental investigations.

Table 1. Physico-chemical properties of the studied catalysts.

Catalyst	Chemical Composition (XRF)			Textural properties			Surface Composition (XPS)		
	atomic ratio			SA	PV	APD	atomic ratio		Mn atom
	Mn/Ce	Mn/Fe	K/Mn	(m^2/g)	(cm^3/g)	(nm)	Mn/Ce	Mn/Fe	AON
M3C1	3.2	-	0.10	184	0.57	27	2.7	-	+3.76
M	-	-	0.13	94	0.34	31	-	-	+3.92
M3F1	-	3.2	0.12	136	0.38	27	-	2.8	+3.82

References

[1]. U.H.R.A. Sheldon, I. Arends, Introduction: Green Chemistry and Catalysis, John Wiley & Sons, Ltd, 2007, Ch. 1, pp. 1–47.

[2]. T. Mallat, A. Baiker, Chem. Rev. 104 (2004) 3037–3058.

[3]. C. Parmeggiani, F. Cardona, Green Chem. 14 (2012) 547–564.

[4]. K. Mori, K. Yamaguchi, T. Hara, T. Mizugaki, K. Ebitani, K. Kaneda, J. Am. Chem. Soc. 124 (2002) 11572–11573.

[5]. D.I. Enache, J.K. Edwards, P. Landon, B. Solsona-Espriu, A.F. Carley, A.A. Herzing, M. Watanabe, C.J. Kiely, D.W. Knight, G.J. Hutchings, Science 311 (2006) 362-365.

[6]. C. Keresszegi, D. Ferri, T. Mallat, A. Baiker, J. Catal. 234 (2005) 64–75.

[7]. N. Dimitratos, A. Villa, D. Wang, F. Porta, D. Su, L. Prati, J. Catal. 244 (2006) 113–121.

[8]. M. Caravati, D. M. Meier, J.-D. Grunwaldt, A. Baiker, J. Catal. 240 (2006) 126–136.

[9]. M. Caravati, J.-D. Grunwaldt, A. Baiker, Catal. Today 126 (2007) 27– 36.

[10]. V.R. Choudhary, J. Rani, J. Prabhas, Green Chem. 9 (2007) 267–272.

[11]. X. Wang, H. Kawanami, S. E. Dapurkar, N.S. Venkataramanan, M. Chatterjee, T. Yokoyama, Y. Ikushima, Appl. Catal. A: Gen. 349 (2008) 86–90.

[12]. C. Y. Ma, B.J. Dou, J.J. Li, J. Cheng, Q. Hu, Z.P. Hao, S.Z. Qiao, Appl. Catal. B: Env. 92 (2009) 202–208.

[13]. Y. Chen, H. Zheng, Z. Guo, C. Zhou, C. Wang, A. Borgna, Y. Yang, J. Catal. 283 (2011) 34–44.

[14]. P.J. Miedziak, Q. He, J.K. Edwards, S.H. Taylor, D.W. Knight, B. Tarbit, C.J. Kiely, G.J. Hutchings, Catal. Today 163 (2011) 47-54.

[15]. J.H.J. Kluytmans, A.P. Markusse, B.F.M. Kuster, G.B. Marin, J.C. Schouten, Catal. Today 57 (2000) 143-1555.

[16]. Y.-C. Son, V. D. Makwana, A. R. Howell, S. L. Suib, Angew. Chem. Int. Ed. Engl. 40 (2001) 4280–4283.

[17]. H. Ji, K. Ebitani, T. Mizugaki, K. Kaneda, Catal. Comm. 3 (2002) 511-517.

[18]. V.D. Makwana, Y.-C. Son, A.R. Howell, S.L. Suib, J. Catal. 210 (2002) 46-52.

[19]. J. Fei, L. Sun, C. Zhou, H. Ling, F. Yan, X. Zhong, Y. Lu, J. Shi, J. Huang, Z. Liu, Nanoscale Res. Lett. 12:23 (2017) 1-9.

[20]. G. Elmaci, D. Ozer, B. Zumreoglu-Karan, Catal. Comm. 89 (2017) 56-59.

[21]. L. Gurrala, A.S. Nagpure, H.R. Gurav, S. Chilukuri, ChemistrySelect 3 (2018) 3751-3761.

[22]. F. Arena, B. Gumina, A.F. Lombardo, C. Espro, A. Patti, L. Spadaro, L. Spiccia, Appl. Catal. B 162 (2015) 260-267.

[23]. Y. Su, L.-C. Wang, Y.-M. Liu, Y. Cao, H.-Y. He, K.-N. Fan, Catal. Comm. 8 (2007) 2181-2185.

[24]. F. Shurz, J.M. Bauchert, T. Merker, T. Shleid, H. Hasse, R. Gläser, Appl. Catal. A 355 (2009) 42-49.

[25]. S. Biswas, A.S. Poyraz, Y. Meng, C.-H. Kuo, C. Guild, M. Tripp, S.L. Suib, Appl. Catal. B. 165 (2015) 731–741.

[26]. T. Qinghu, W. Chengming, H. Xiaona, Y. Yanhui, Chin. J. Catal. 30 (2009) 207-212.

[27]. T. Sato, T. Komanaya, Catal. Comm. 10 (2009) 1095-1098.

[28]. X. Shen, A.M. Morey, J. Liu, Y. Ding, J. Cai, J. Durand, Q. Wang, W. Wen, W.A. Hines, J.C. Hanson, J. Bai, A.I. Frenkel, W. Reiff, M. Aindow, S.L. Suib, J. Phys. Chem. C 115 (2011) 21610-21619.

[29]. F. Arena, B. Gumina, C. Cannilla, L. Spadaro, A. Patti, L. Spiccia, Appl. Catal. B 170 (2015) 233–240.

[30]. F. Brühne, E. Wright, Benzaldehyde, American Cancer Society, 2011.

[31]. F. Ferrante, A. Prestianni, D. Duca, J. Phys. Chem. C 118 (2014) 551– 558.

[32]. R. Cortese, R. Schimmenti, F. Ferrante, A. Prestianni, D. Decarolis, D. Duca, J. Phys. Chem. C 121 (2017) 13606–13616.

[33]. R. Schimmenti, R. Cortese, L. Godina, A. Prestianni, F. Ferrante, D. Duca, D. Yu. Murzin, J. Phys. Chem. C 121 (2017) 14636–14648.

[34]. A. Prestianni, M. Crespo-Quesada, R. Cortese, F. Ferrante, L. Kiwi- Minsker, D. Duca, J. Phys. Chem. C 118 (6) (2014) 3119–3128.

[35]. H. Yuan, J. Chen, Y. Guo, H. Wang, P. Hu, J. Phys. Chem. C 122 (2018) 25365−25373.

[36]. D. Duca, F. Ferrante, G. La Manna, J. Phys. Chem. C 111 (2007) 5402– 5408.

[37]. V. D'Anna, D. Duca, F. Ferrante, G. La Manna, Phys. Chem. Chem. Phys. 11 (2009) 4077–4083.

[38]. V. D'Anna, D. Duca, F. Ferrante, G. La Manna, Phys. Chem. Chem. Phys. 12 (2010) 1323–1330.

[39]. A. Prestianni, F. Ferrante, E. M. Sulman, D. Duca, J. Phys. Chem. C 118 (2014) 21006–21013.

[40]. R. Schimmenti, R. Cortese, F. Ferrante, A. Prestianni, D. Duca, Phys. Chem. Chem. Phys. 18 (2016) 1750–1757.

[41]. F. Ferrante, A. Prestianni, R. Cortese, R. Schimmenti, D. Duca, J. Phys. Chem. C 120 (2016) 12022–12031.

[42]. A. Prestianni, R. Cortese, F. Ferrante, R. Schimmenti, D. Duca, S. Hermans, D. Yu. Murzin, Top. Catal. 59 (2016) 1178–1184.

[43]. Y. Zhao, D. G. Truhlar, J. Chem. Phys. 125 (2006) 194101.

[44]. Y. Zhao, D.G. Truhlar, Theor. Chem. Account 120 (2008) 215-241.

[45]. Y. Sun, H. Chen, J. Chem. Theory Comp. 9 (2013) 4735-4743.

[46]. Y. Sun, H. Chen, J. Chem. Theory Comp. 10 (2014) 579-588.

[47]. L. Hu, H. Chen, J. Chem. Theory Comp. 11 (2015) 4601-4614.

[48]. M. Dolg, U. Wedig, H. Stoll, H. Preuss, J. Chem. Phys. 86 (1987) 1730-1734.

[49]. J.M.L. Martin, A. Sundermann, J. Chem. Phys. 114 (2001) 3408-3420.

[50]. M. J. Frisch, G.W. Trucks, H.B. Schlegel, G.E. Scuseria, M.A. Robb, R. Cheeseman, G. Scalmani, V. Barone, B. Mennucci, G. A. Petersson, H. Nakatsuji, M. Caricato, X. Li, H. P. Hratchian, A. F. Izmaylov, J. Bloino, G. Zheng, J. L. Sonnenberg, M. Hada, M. Ehara, Toyota, R. Fukuda, J. Hasegawa, M. Ishida, T. Nakajima, Y. Honda, O. Kitao, H. Nakai, T. Vreven, J.J.A. Montgomery, J.E. Peralta, F. Ogliaro, M. Bearpark, J.J. Heyd, E. Brothers, K.N. Kudin, V.N. Staroverov, R. Kobayashi, J. Normand, K. Raghavachari, A. Rendell, J.C. Burant, S.S. Iyengar, J. Tomasi, M. Cossi, N. Rega, J.M. Millam, M. Klene, J.E. Knox, J.B. Cross, V. Bakken, C. Adamo, J. Jaramillo, R. Gomperts, R.E. Stratmann, O. Yazyev, A.J. Austin, R. Cammi, C. Pomelli, J.W. Ochterski, R.L. Martin, K. Morokuma, V.G. Zakrzewski, G. A. Voth, P. Salvador, J.J. Dannenberg, S. Dapprich, A.D. Daniels, Ö. Farkas, J.B. Foresman, J.V. Ortiz, J. Cioslowski, D.J. Fox, *Gaussian 09 Revision D.01*, Gaussian Inc. Wallingford CT 2009.

[51]. S. Boys, F. Bernardi, Mol. Phys. 19 (1970) 553–566.

[52]. F. Arena, R. Di Chio, B. Fazio, C. Espro, L. Spiccia, A. Palella, L. Spadaro, Appl. Catal. B Environ. 210 (2017) 14–22.

[53]. F. Arena, G. Trunfio, J. Negro, B. Fazio, and L. Spadaro, Chem. Mater. 19 (2007) 2269–2276.

[54]. K. Selvakumar, S.M.S. Kumar, R. Thangamuthu, K. Ganesan, P. Murugan, P. Rajput, S.N. Jha, D. Bhattacharyya, J. Phys. Chem. C 119 (2015) 6604–6618.

[55]. S. Liang, F. Teng, G. Bulgan, R. Zong, Y. Zhu, J. Phys. Chem. C 112 (2008) 5307-5315.

Supplementary Material